PROCEEDINGS OF SCIENCE

Search for new phenomena in high-mass final states with a photon and a jet from *pp* collisions at 13 TeV with the ATLAS detector

Jonathan D. Bossio Sola, on behalf of the ATLAS Collaboration*
Universidad de Buenos Aires †
E-mail: jbossios@cern.ch

A search is performed for new phenomena in events having a photon with high transverse momentum and a jet collected in 36.7 fb^{-1} of proton-proton collisions at a centre-of-mass energy of 13 TeV recorded with the ATLAS detector at the LHC. The invariant mass distribution of the leading photon and jet is examined to look for the resonant production of new particles or the presence of new high-mass states beyond the SM. No significant deviation from the background-only hypothesis is observed and cross-section limits for generic Gaussian-shaped resonances are extracted. Excited quarks hypothesised in quark compositeness models and high-mass states predicted in quantum black hole models with extra dimensions are also examined in the analysis. The observed data exclude, at 95% confidence level, the mass range below 5.3 TeV for excited quarks and 7.1 TeV (4.4 TeV) for quantum black holes in the Arkani-Hamed-Dimopoulos-Dvali (Randall-Sundrum) model with six (one) extra dimensions.

Corfu Summer Institute 2018 "School and Workshops on Elementary Particle Physics and Gravity" (CORFU2018)
31 August - 28 September, 2018
Corfu, Greece

*Speaker.
†Now at McGill University

PoS(CORFU2018)051

1. Introduction

Prompt photons in association with jets are copiously produced at the Large Hadron Collider (LHC), through either Compton scattering of a quark and a gluon or through quark-antiquark annihilation, as shown in Figure 1. The quark-gluon diagrams account for most of $\gamma+$jet production since those are favoured over the quark-antiquark diagrams due to the parton distribution functions (PDFs). $\gamma+$jet events can also be produced at the LHC through gluon annihilation, but this is an NNLO process (Figure 2 shows the lowest order Feynman diagram).

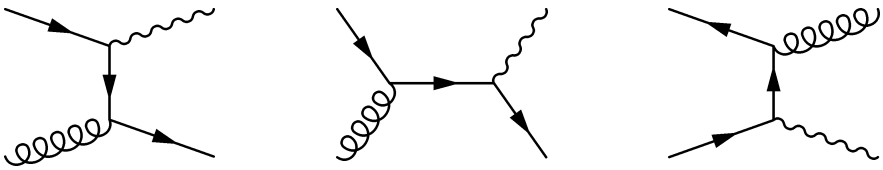

Figure 1: Standard Model diagrams contributing to $\gamma+$jet production at tree level.

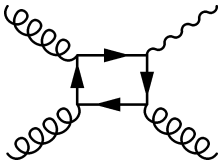

Figure 2: Lowest order $gg \to \gamma+$jet diagram in the Standard Model.

The γ + jet(s) final state provides also a sensitive probe for a class of phenomena beyond the Standard Model (SM) that could manifest themselves in the high end of the invariant mass spectrum of the $\gamma+$jet system ($m_{\gamma j}$). The search is performed by looking for localised excesses of events in the $m_{\gamma j}$ distribution with respect to the SM prediction. Two classes of benchmark signal models are considered. The first class consists of specific beyond the SM (BSM) models and the second one is based on generic Gaussian-shaped mass distributions.

The BSM signals are implemented in Monte Carlo (MC) simulation and appear as broad peaks in the $m_{\gamma j}$ spectrum. In this search, two scenarios are considered: quarks as composite particles and extra spatial dimensions. In the first case, if quarks are composed of more fundamental constituents bound together by some unknown interaction, new effects should appear depending on the value of the compositeness scale Λ. A quark substructure could explain the origin of the three generations of quarks as well as their various masses and behaviours under weak interactions. In particular, if Λ is sufficiently smaller than the centre-of-mass energy, excited quark (q^*) states may be produced in high-energy pp collisions at the LHC [1–3]. The q^* production at the LHC could result in a resonant peak at the mass of the q^* (m_{q^*}) in the $m_{\gamma j}$ distribution if the q^* can decay into a photon and a quark. The present search considers excited up (u^*) and down (d^*) quarks, and only the SM gauge interactions for q^* production.

In the second scenario, the existence of extra spatial dimensions (EDs) is assumed to provide a solution to the hierarchy problem [4–6]. Certain types of ED models predict the fundamental

Planck scale M^* in the $4+n$ dimensions (n being the number of extra spatial dimensions) to be at the TeV scale, and thus accessible in pp collisions at $\sqrt{s} = 13$ TeV at the LHC. In such a TeV-scale M^* scenario of the extra dimensions, quantum black holes (QBHs) may be produced at the LHC as a continuum above the threshold mass (M_{th}) and then decay into a small number of final-state particles including photon-quark/gluon pairs before they are able to thermalise [7–10]. In this case a broad resonance-like structure could be observed just above M_{th} on top of the SM $m_{\gamma j}$ distribution. The M_{th} value for QBH production is taken to be equal to M^* while the maximum allowed QBH mass is set to either $3M^*$ or the LHC pp centre-of-mass energy of 13 TeV, whichever is smaller. The upper bound on the mass ensures that the QBH production is far from the "thermal" regime, where the classical description of the black hole and its decay into high-multiplicity final states should be used. In this analysis, the extra-dimensions model proposed by Arkani-Hamed, Dimopoulous and Dvali (ADD) [11] with $n = 6$ flat EDs, and the one by Randall and Sundrum (RS1) [12] with $n = 1$ warped ED are considered. Figure 3 shows the expected cross-section times branching ratio to a photon and a jet in pp collisions at $\sqrt{s} = 13$ TeV for all the BSM signals considered in this search.

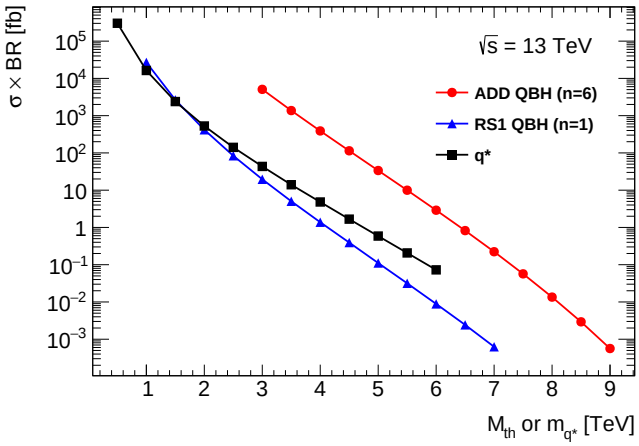

Figure 3: Production cross-section times $\gamma+$jet branching ratio for a excited quark q^* and two different non-thermal quantum black hole models (RS1, ADD) as a function of the q^* mass or the mass threshold for black hole production M_{th}, in pp collisions at $\sqrt{s} = 13$ TeV. The q^* cross-section is computed at leading order in α_s with the PYTHIA 8.186 event generator [13]. The excited quark model assumes that the compositeness scale is equal to the excited quark mass m_{q^*}, and that gauge interactions of excited quarks are like those in the SM, with the $SU(3)$, $SU(2)$, and $U(1)$ coupling multipliers fixed to $f_s = f = f' = 1$. The quantum black hole cross-sections are obtained with the QBH 2.02 event generator [14]. In the RS1 and ADD quantum black hole models the number of extra spatial dimensions is $n = 1$ and $n = 6$, respectively. The maximum mass for the black hole production is set to the pp centre-of-mass energy or to $3M_{\text{th}}$ if $M_{\text{th}} < \sqrt{s}/3$. The cross-sections are calculated in 0.5 TeV mass steps (dots) and interpolated with a continuous function (solid lines) [15].

The second class of benchmark models, based on a generic Gaussian-shaped mass distribution with different values of its mean and standard deviation, provides a generic interpretation for the presence of signals with different Gaussian widths, ranging from a resonance with a width similar

to the reconstructed $m_{\gamma j}$ resolution of $\sim 2\%$ to wide resonances with a width up to 15%. This approach is considered since new physics is not only limited to particular models but may appear in unexpected places with an unexpected form. Hence, the search presented here is ultimately model independent and is sensitive to any localised excess which may be caused by any BSM process with a $\gamma+$jet final state.

The ATLAS [16] and CMS [17] experiments at the LHC have performed searches for excited quarks in the $\gamma+$jet final state using pp collision data recorded at $\sqrt{s} = 7$ TeV [18], 8 TeV [19, 20] and 13 TeV [15]. In the ATLAS searches, limits for generic Gaussian-shaped resonances were obtained at 7, 8 and 13 TeV while a limit for QBHs in the ADD model ($n = 6$) was first obtained at 8 TeV. The ATLAS search at 13 TeV with data taken in 2015 was further extended to constrain QBHs in the RS1 model ($n = 1$). The dijet resonance searches at ATLAS [21, 22] and CMS [23] using pp collisions at $\sqrt{s} = 13$ TeV also set limits on the production cross-sections of excited quarks and QBHs.

A search based on the full 2015 and 2016 dataset recorded with the ATLAS detector, corresponding to 36.7 fb^{-1} of pp collisions at $\sqrt{s} = 13$ TeV is performed [24]. The search presented here complements the dijet results and provides an independent check for the presence of BSM signals in different decay channels.

2. ATLAS detector

The ATLAS detector at the LHC is a multi-purpose, forward-backward symmetric detector[1] with almost full solid angle coverage, and is described in detail elsewhere [20, 21]. Most relevant for this analysis are the inner detector (ID) and the calorimeter system composed of electromagnetic (EM) and hadronic calorimeters. The ID consists of a silicon pixel detector, a silicon microstrip tracker and a transition radiation tracker, all immersed in a 2 T axial magnetic field, and provides charged-particle tracking in the range $|\eta| < 2.5$. The electromagnetic calorimeter is a lead/liquid-argon (LAr) sampling calorimeter with accordion geometry. The calorimeter is divided into a barrel section covering $|\eta| < 1.475$ and two endcap sections covering $1.375 < |\eta| < 3.2$. For $|\eta| < 2.5$ it is divided into three layers in depth, which are finely segmented in η and ϕ. In the region $|\eta| < 1.8$, an additional thin LAr presampler layer is used to correct for fluctuations in the energy losses in the material upstream of the calorimeters. The hadronic calorimeter is a sampling calorimeter composed of steel/scintillator tiles in the central region ($|\eta| < 1.7$), while copper/LAr modules are used in the endcap ($1.5 < |\eta| < 3.2$) regions. The forward region ($3.1 < |\eta| < 4.9$) is instrumented with copper/LAr and tungsten/LAr calorimeter modules optimised for electromagnetic and hadronic measurements, respectively. Surrounding the calorimeters is a muon spectrometer that includes three air-core superconducting toroidal magnets and multiple types of tracking chambers, providing precision tracking for muons within $|\eta| < 2.7$ and trigger capability within $|\eta| < 2.4$. A dedicated two-level trigger system is used for the online event selection [25].

[1] ATLAS uses a right-handed coordinate system with its origin at the nominal interaction point (IP) in the centre of the detector and the z-axis along the beam pipe. The x-axis points from the IP to the centre of the LHC ring, and the y-axis points upwards. Cylindrical coordinates (r,ϕ) are used in the transverse plane, ϕ being the azimuthal angle around the z-axis. The pseudorapidity is defined in terms of the polar angle θ as $\eta = \ln\tan(\theta/2)$. Angular distance is measured in units of $\Delta R \equiv \sqrt{(\Delta\eta)^2 + (\Delta\phi)^2}$.

Events are selected using a first-level trigger implemented in custom electronics, which reduces the event rate to a design value of 100 kHz using a subset of the detector information. This is followed by a software-based trigger that reduces the accepted event rate to 1 kHz on average by refining the first-level trigger selection.

3. Background processes

Events with a real high-p_{T} photon and one or more jets can also be produced if a parton shower quark radiates off a photon, or when a hadron in a multijet event decays producing a photon. While such photons tend to appear near or inside jets and thus fail isolation criteria, the much larger multijet cross-sections imply that such fragmentation production can be a non-negligible contribution to isolated $\gamma+$jet signatures.

Events without a photon at parton level can also pass the event selection, and are called "fakes". This is a smaller component of background photon candidates and is due to hadrons producing in the detector energy deposits that have characteristics similar to those of real photons. By far, the dominant process is from dijet events, in which one of the jets pass the photon selection.

4. Event selection

Photons are reconstructed from clusters of energy deposits in the EM calorimeter as described in [26]. A photon candidate is classified depending on whether the EM cluster is associated with a conversion track candidate reconstructed in the ID. If no ID track is matched, the candidate is considered as an unconverted photon. If the EM cluster is matched to either a conversion vertex formed from two tracks constrained to originate from a massless particle or a single track with its first hit after the innermost layer of the pixel detector, the candidate is considered to be a converted photon. Both the converted and unconverted photon candidates are used in the analysis. Photon candidates are required to have $E_{\mathrm{T}}^{\gamma} > 25\,\mathrm{GeV}$ and $|\eta^{\gamma}| < 2.37$ and satisfy the "tight" identification criteria, designed to lower significantly the contribution from background, defined in [26]. Photons are identified based on the width of the energy deposits in the first two layers of the EM calorimeter and the energy leakage into the hadronic calorimeter. To further reduce the contamination from $\pi^0 \to \gamma\gamma$ or other neutral hadrons decaying into photons, the photon candidates are required to be isolated from other energy deposits in an event. The calorimeter isolation variable $E_{\mathrm{T,iso}}$ is defined as the sum of the E_{T} of all positive-energy topological clusters reconstructed within a cone of $\Delta R = 0.4$ around the photon direction excluding the energy deposits in an area of size $\Delta\eta \times \Delta\phi = 0.125 \times 0.175$ centred on the photon cluster. The photon energy expected outside the excluded area is subtracted from the isolation energy while the contributions from pile-up and the underlying event are subtracted event by event [27]. The photon candidates are required to have $E_{\mathrm{T,iso}}^{\gamma} = E_{\mathrm{T,iso}} - 0.022 \times E_{\mathrm{T}}^{\gamma}$ less than 2.45 GeV [24]. The efficiency for the signal photon selection varies from $(90 \pm 1)\%$ to $(83 \pm 1)\%$ for signal events with masses from 1 to 6 TeV. The dependency on the signal mass is mainly from the efficiency of the tight identification requirement while the isolation selection efficiency is approximately $(99 \pm 1)\%$ over the full mass range.

Jets are reconstructed from topological clusters calibrated at the EM scale using the anti-k_t algorithm with a radius parameter $R = 0.4$. The jets are calibrated to the hadronic energy scale

by applying corrections derived from MC simulation and in situ measurements of relative jet response obtained from Z+jets, γ+jets and multijet events at $\sqrt{s} = 13$ TeV [28]. Jets from pile-up interactions are suppressed by applying the jet vertex tagger [29], using information about tracks associated with the hard-scatter and pile-up vertices, to jets with $p_{\mathrm{T}}^{\mathrm{jet}} < 60$ GeV and $|\eta^{\mathrm{jet}}| < 2.4$. In order to remove jets due to calorimeter noise or non-collision backgrounds, events containing at least one jet failing to satisfy the "loose" quality criteria defined in [30] are discarded. Jets passing all the requirements and with $p_{\mathrm{T}}^{\mathrm{jet}} > 20$ GeV and $|\eta^{\mathrm{jet}}| < 4.5$ are considered in the rest of the analysis. Since a photon can be mistaken as a jet, jet candidates in a cone of $\Delta R = 0.4$ around a photon are not considered.

This analysis selects events based on an unprescaled single-photon trigger requiring at least one photon candidate with $E_{\mathrm{T}}^{\gamma} > 140$ GeV which satisfies loose identification conditions [26] based on the shower width in the second sampling layer of the EM calorimeter and the energy leakage into the hadronic calorimeter. Selected events are required to contain at least one primary vertex with two or more tracks with $p_{\mathrm{T}} > 400$ MeV, to further reject events due to non-collision backgrounds. Photon candidates are required to satisfy the "tight" identification and isolation conditions discussed above. The kinematic requirements for the highest-E_{T} photon in the events are tightened to $E_{\mathrm{T}}^{\gamma} > 150$ GeV and $|\eta^{\gamma}| < 1.37$. The E_{T}^{γ} requirement is used to select events with nearly 100% trigger efficiency, while the η^{γ} requirement is imposed to enhance the signal-to-background ratio.

Moreover, an event is rejected if there is any jet with $p_{\mathrm{T}}^{\mathrm{jet}} > 30$ GeV within $\Delta R < 0.8$ around the photon to further avoid possible contamination from nearby jets to the photon isolation cone, which might lead to a bias in the calibration of the photon. The number of signal and background events with additional tight and isolated photons with $E_{\mathrm{T}}^{\gamma} > 150$ GeV is negligible, and therefore these events are accepted. The $\gamma+$jet system is formed from the highest-E_{T} photon and the highest-p_{T} jet in the event. Finally, the highest-p_{T} jet in the event is required to have $p_{\mathrm{T}}^{\mathrm{jet}} > 60$ GeV and the pseudorapidity difference between the photon and the jet ($\Delta\eta_{\gamma j} \equiv |\eta^{\gamma} - \eta^{\mathrm{jet}}|$) must be less than 1.6 to enhance signals over the $\gamma+$jet background.

5. Signal modelling

The signal model is built starting from the probability density function (pdf) of the $m_{\gamma j}$ distribution $f_{\mathrm{sig}}(m_{\gamma j})$ at the reconstruction level. For a Gaussian-shaped resonance with mass m_{G}, the $m_{\gamma j}$ pdf is modelled by a normalised Gaussian distribution with the mean located at $m_{\gamma j} = m_{\mathrm{G}}$. The standard deviation of the Gaussian distribution is chosen to be 2%, 7% or 15% of m_{G}, where 2% approximately corresponds to the effect of the detector resolution on the reconstruction of the photon–jet invariant mass. For the q^* and QBH signals, the $m_{\gamma j}$ pdfs are created from the normalised reconstructed $m_{\gamma j}$ distributions after applying the selection requirements described in Section 4 using simulated MC events, and a kernel density estimation technique [31] is applied to smooth the distributions. The signal pdfs for intermediate mass points at which signal events were not generated are obtained from the simulated samples by using a moment-morphing method [32]. Figure 4 shows the $m_{\gamma j}$ distributions from the MC sample for the q^* and RS1 QBH models for different signal masses.

The signal template for the q^* and QBH signals is then constructed as $f_{\mathrm{sig}}(m_{\gamma j}) \times (\sigma_{\mathrm{S}} \cdot B \cdot A \cdot \varepsilon) \times \mathscr{L}_{\mathrm{int}}$, where f_{sig} is scaled by the product of the cross-section and the branching ratio to a photon

and a quark or gluon ($\sigma_S \cdot B$), acceptance (A), selection efficiency (ε) and the integrated luminosity ($\mathscr{L}_{\text{int}}$) for the data sample. The product of the acceptance and the efficiency ($A \cdot \varepsilon$) is found to be about 50% for all q^* and QBH models, varying only by a few percent with m_{q^*} or M_{th}.

Experimental uncertainties in the signal yield arise from uncertainties in the luminosity ($\pm 3.2\%$), photon identification efficiency ($\pm 2\%$), trigger efficiency ($\pm 1\%$ as measured in [33]) and pile-up dependence ($\pm 1\%$). The impact of the uncertainties in the photon isolation efficiency, photon and jet energy scales is negligible. A 1% uncertainty in the signal yield is included to account for the statistical error in the acceptance and selection efficiency estimates due to the limited size of the MC signal samples. The impact of the PDF uncertainties on the signal acceptance is found to be negligible compared to the other uncertainties. The photon and jet energy resolution uncertainties ($\pm 2\%$ of the mass) are accounted for as a variation of the width for the Gaussian-shaped signals. The impact of the resolution uncertainty on intrinsically large width signals is found to be negligible and thus not included in the signal models for q^* and QBH.

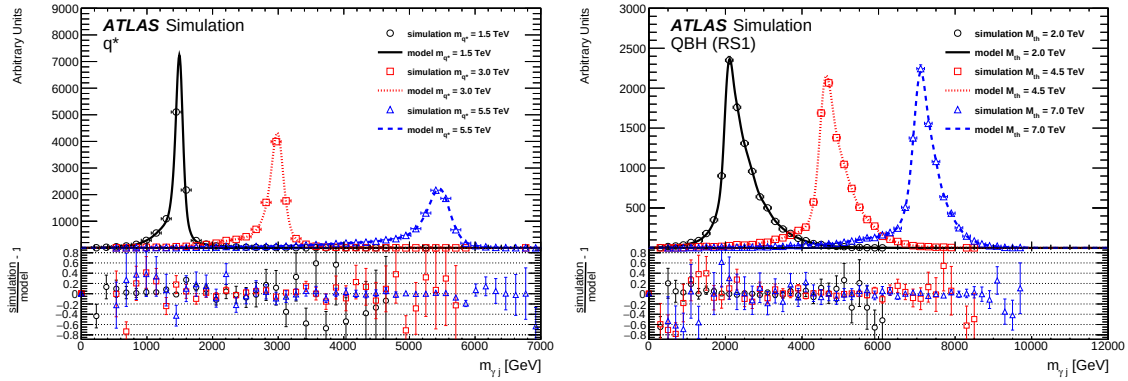

(a) (b)

Figure 4: The $m_{\gamma j}$ distributions from the MC sample for (a) q* and (b) RS1 QBH models for different signal masses (m_{q^*} and M_{th}). For each distribution, the model used in the statistical interpretation of the data is also shown. The bottom panels for each figure show the accuracy of the model in describing the invariant mass distributions for the different signals and for different masses [34].

6. Background modelling

The $m_{\gamma j}$ distribution of the background is modelled using a functional form from the following family of functions:

$$f_{\text{bg}}(x) = N(1-x)^p x^{\sum_{i=0}^{k} a_i (\log x)^i}, \tag{6.1}$$

where x is defined as $m_{\gamma j}/\sqrt{s}$, p and a_i are free parameters, and N is a normalisation factor.

The goodness of a given functional form in describing the background is quantified based on the potential bias introduced in the fitted number of signal events. To quantify this bias the functional form under test is used to perform a signal + background fit to a large sample of background events obtained with the next-to-leading-order JETPHOX v1.3.1_2 [35] program. The parton-level JETPHOX calculations do not account for effects from hadronisation, the underlying event and the

detector resolution. Therefore, the nominal JETPHOX prediction is corrected by calculating the ratio of reconstructed jet p_{T} to parton p_{T} in a $\gamma+$jet sample produced with the SHERPA 2.1.1 [36] event generator and applying the parametrised ratio to the JETPHOX parton p_{T}. In addition, an $m_{\gamma j}$-dependent correction is applied to the JETPHOX prediction to account for the contribution from multijet events where one of the jets is misidentified as a photon. This correction is estimated from data as the inverse of the purity, defined as the fraction of real $\gamma+$jet events in the selected sample. The purity is measured by exploiting the difference between the shapes of the $E^{\gamma}_{\mathrm{T,\,iso}}$ distributions of real photons and jets faking photons. The purity is estimated by performing a two-component template fit to the $E^{\gamma}_{\mathrm{T,\,iso}}$ distribution in bins of $m_{\gamma j}$. The templates of real- and fake-photon isolation distributions are obtained from MC (SHERPA) simulation and from data control samples, respectively. The $E^{\gamma}_{\mathrm{T,\,iso}}$ variable for real photons from SHERPA simulation is corrected to account for the observed mismodelling in the description of isolation profiles between data and MC events in a separate control sample. The template for fake photons is derived in a data sample where the photon candidate fails to satisfy the tight identification criteria but fulfills a looser set of identification criteria. Figure 5 shows the $E^{\gamma}_{\mathrm{T,\,iso}}$ distribution of events within the range $1.0 < m_{\gamma j} < 1.1$ TeV, superimposed on the best-fit result. This procedure is repeated in every bin of the $m_{\gamma j}$ distribution and the resulting estimate of the purity is shown as a function of $m_{\gamma j}$ in Figure 6. The uncertainty in the measured purity includes both statistical and systematic components. The latter are estimated by recomputing the purity using different data control samples for the fake-photon template or alternative templates for real photons obtained from PYTHIA simulation or removing the data-to-MC corrections applied to $E^{\gamma}_{\mathrm{T,\,iso}}$ in the SHERPA sample and by symmetrising the variations. The measured purity is approximately constant at 93% over the $m_{\gamma j}$ range above 500 GeV, indicating that the fake-photon contribution does not depend significantly on $m_{\gamma j}$.

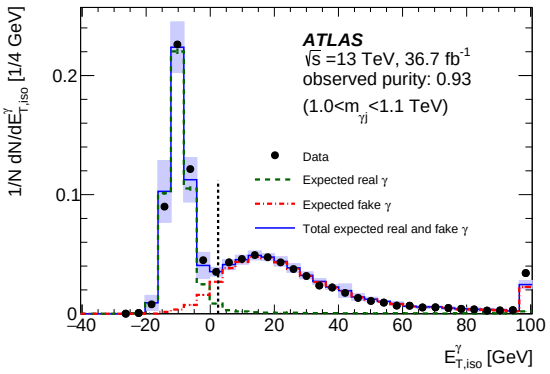

Figure 5: Distribution of $E^{\gamma}_{\mathrm{T,\,iso}} = E_{\mathrm{T,\,iso}} - 0.022 \times E^{\gamma}_{\mathrm{T}}$ for the photon candidates in events with $1.0 < m_{\gamma j} < 1.1$ TeV, and the comparison with the result of the template fit. Real- and fake-photon components determined by the fit are shown by the green dashed and red dot-dashed histograms, respectively, and the sum of the two components is shown as the solid blue histogram. The shaded band shows the systematic uncertainties in the real- plus fake-photon template. The last bin of the distribution includes overflow events. The vertical dashed line corresponds to the isolation requirement cut used in the analysis [24].

The $m_{\gamma j}$ distribution in data compared to the corrected JETPHOX $\gamma+$jet prediction normalised

to data in the $m_{\gamma j} > 500\,\text{GeV}$ region is shown in Figure 6. Theoretical uncertainties in the JETPHOX prediction are computed by considering the variations induced by $\pm 1\sigma$ of the NNPDF 2.3 PDF uncertainties, by switching between the nominal NNPDF 2.3 and CT10 or MSTW2008 PDF sets, by the variation of the value of the strong coupling constant by ± 0.002 around the nominal value of 0.118 and by the variations of the renormalisation, factorisation and fragmentation scales between half and twice the photon transverse momentum. The differences between data and the corrected JETPHOX prediction shown in Figure 6 are well within the uncertainties associated with the perturbative quantum chromodynamics prediction.

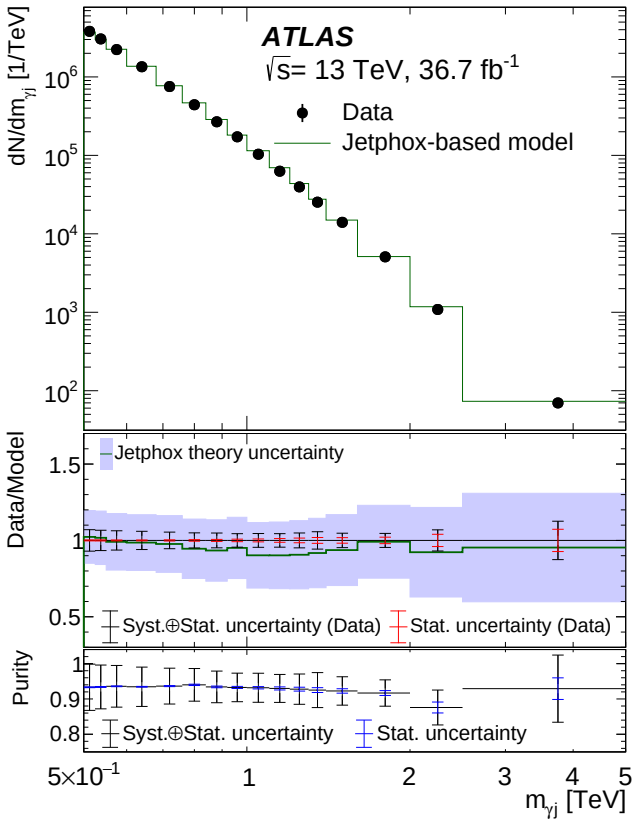

Figure 6: Distribution of the invariant mass of the γ + jet system as measured in the γ+jet data (dots), compared with the JETPHOX (green histogram) γ+jet predictions. The JETPHOX distribution is obtained after correcting the parton-level spectrum for showering, hadronisation and detector resolution effects as described in the text. The JETPHOX spectrum is normalised to the data in the $m_{\gamma j}$ range above 500 GeV. The ratio of the data to JETPHOX prediction as a function of $m_{\gamma j}$ is shown in the middle panel (green histogram): the theoretical uncertainty is shown as a shaded band. The statistical uncertainty from the data sample and the sum of the statistical uncertainty plus the systematic uncertainty from the background subtraction are shown as inner and outer bars respectively. The measured γ+jet purity as a function of $m_{\gamma j}$ is presented in the bottom panel: the statistical uncertainty of the purity measurement is reported as the inner error bar while the total uncertainty is shown as the outer error bar [24].

The number of signal events extracted by the signal + background fit to the pure background model described above is called the "spurious signal" and it is used to select the optimal functional form and the $m_{\gamma j}$ range of the fit. In order to account for the assumption that the corrected JETPHOX prediction itself is a good representation of the data, the fit is repeated on modified samples obtained by changing the nominal shape to account for several effects: firstly, the nominal distribution is corrected to follow the envelope of the changes introduced above (related to the PDF choice, the strong coupling constant and, the renormalisation, factorisation and fragmentation scales); secondly the corrections for the hadronisation, underlying event and detector effects are removed; and finally the corrections for the photon purity are changed within their estimated uncertainties. The largest absolute fitted signal from all variations of the nominal background sample discussed above is taken to be the spurious signal.

The spurious signal is evaluated at a number of hypothetical masses over a large search range. It is required to be less than 40% of the background statistical uncertainty, as quantified by the statistical uncertainty of the fitted spurious signal, anywhere in the investigated search range. Functional forms that cannot meet this requirement are rejected. For different signal models, the functional form and fit range are determined separately. To further consolidate the choice of nominal background functional form, an F-test [37] is performed to determine if the change in the χ^2 value obtained by fitting the JETPHOX sample with an additional parameter is significant.

Given the fit range determined by the spurious signal test, the search is performed for the q^* (RS1 and ADD QBH) signal within the $m_{\gamma j}$ range above 1.5 (2.0 and 3.0) TeV, to account for the width of the expected signal. The estimated spurious signal for the selected functional form is converted into a spurious-signal cross-section (σ_{spur}), shown in Figure 7 for all signal models, which is included as the uncertainty due to background modelling in the statistical analysis.

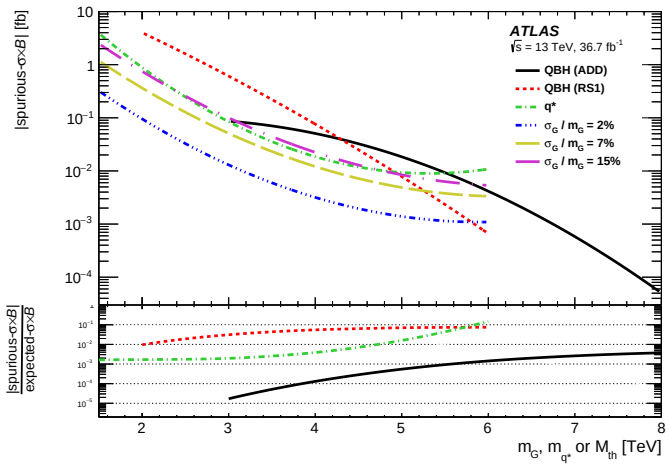

Figure 7: Spurious signal cross-section as a function of $m_{\gamma j}$ for all signal models under test. The bottom panel reports the ratios of the spurious signal cross-section over the expected signal cross-section for q^* and QBH signals [34].

A similar test is performed to determine the functional form and fit ranges for the Gaussian-shaped signal with a 15% width. The test indicates that the same functional form and fit range as those used for the q^* signal are optimal for a wide-width Gaussian signal. The same functional

form and mass range is used for all the Gaussian signals.

7. Results

The photon–jet invariant mass distributions obtained from the selected data are shown for the q^* model in Figure 8, together with the background-only fits and an example of the expected distribution from the background plus signal model under test. No significant deviation from the background-only prediction is observed in any of the distributions. The most significant excess is observed at 1.8 TeV for the assumption of a 2%-width Gaussian model for a local significance of 2.1 standard deviations.

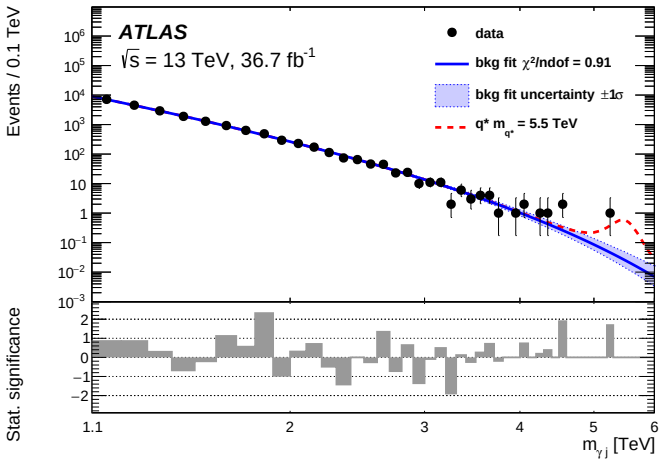

Figure 8: Distributions of the invariant mass of the γ + jet system of the observed events (dots) in 36.7fb^{-1} of data at $\sqrt{s} = 13$ TeV and fits to the data (solid lines) under the background-only hypothesis for a search in the excited quark model. The $\pm 1\sigma$ uncertainty in the background prediction originating from the uncertainties in the fit function parameter values is shown as a shaded band around the fit. The predicted signal distribution (dashed line) for the q^* model with m_{q^*} = 5.5 TeV is shown on top of the background predictions. The bottom panels show the bin-by-bin significances of the data–fit differences, considering only statistical uncertainties [24].

Limits are placed at 95% CL on the visible cross-section in the case of generic Gaussian-shaped resonances and on the production cross-section times branching ratio to a photon and a quark or gluon for the q^* and QBH signals. The results are shown in Figure 9. The Gaussian signals are excluded for visible cross-sections above 0.25–1.1 fb (0.08–0.2 fb), depending on the width, at a mass m_G of 3 TeV (5 TeV). In the case of the benchmark signal models considered in this analysis, the presence of a signal with a mass below 5.3, 4.4 and 7.1 TeV for the excited quarks, RS1 and ADD QBHs, respectively, can be excluded at 95% CL. The limits improve on those in [15] by about 0.9, 0.6 and 0.9 TeV, respectively for the q^*, RS1 and ADD QBHs.

8. Conclusions

A search is performed for new phenomena in events having a photon with high transverse momentum and a jet collected in 36.7 fb^{-1} of pp collision data at a centre-of-mass energy of $\sqrt{s} =$

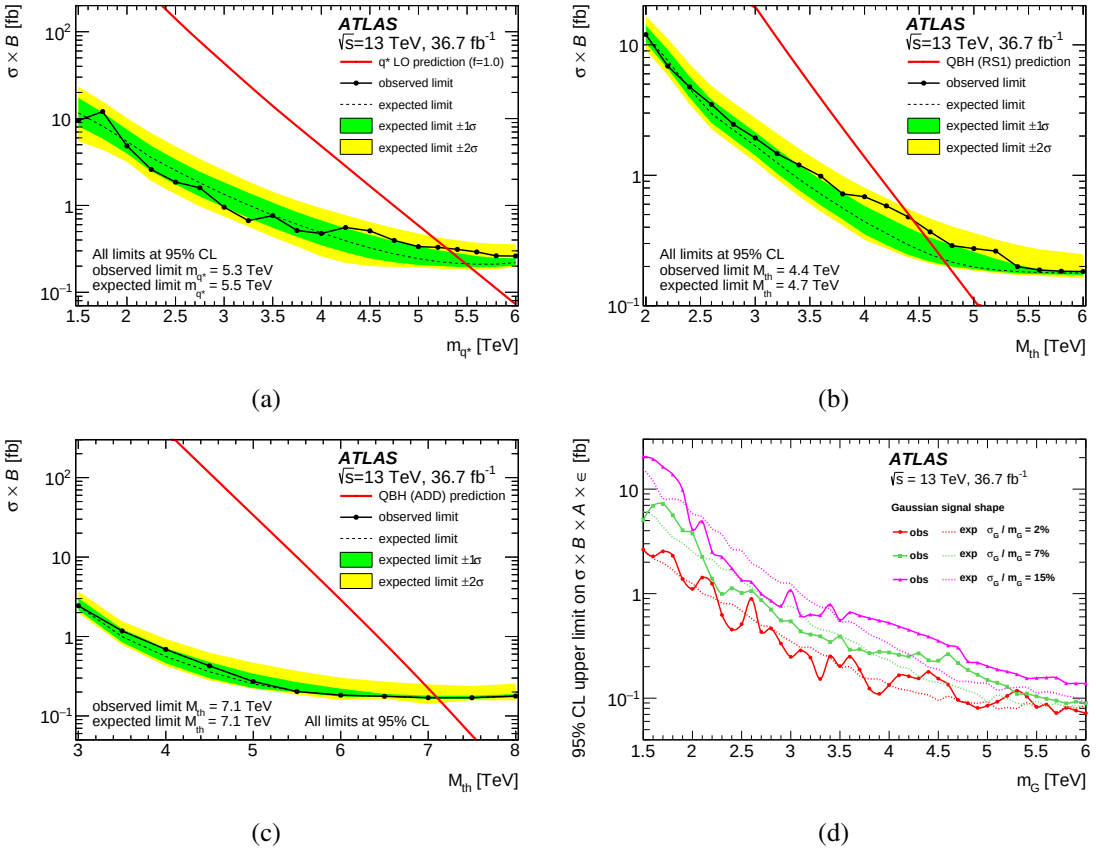

Figure 9: Observed (solid lines with dots) and expected (dotted lines) 95% CL upper limits in 36.7 fb^{-1} of data at $\sqrt{s} = 13$ TeV on the production cross-section times branching ratio to a photon and a quark or gluon for the (a) q^*, (b) QBH (RS1) with one extra dimension and (c) QBH (ADD) with six extra dimensions models; and on the visible cross-sections $\sigma_S \cdot B \cdot A \cdot \varepsilon$ as a function of the mass m_G of the Gaussian resonances with three different Gaussian widths between 2% and 15%. The limits are placed as a function of m_{q^*} for the q^* and M_{th} for the QBH signals. The dashed lines correspond to the limits expected if a signal is absent. For BSM signals, these are shown together with the $\pm 1\sigma$ and $\pm 2\sigma$ intervals represented by the green and yellow bands, respectively. The theoretical predictions of $\sigma_S \cdot B$ for the respective BSM signals are shown by the red solid lines [24].

13 TeV recorded with the ATLAS detector at the LHC. The invariant mass distribution of the γ + jet system above 1.1 TeV is used in the search for localised excesses of events. No significant deviation is found. Limits are set on the visible cross-section for generic Gaussian-shaped resonances and on the production cross-section times branching ratio for signals predicted in models of excited quarks or quantum black holes. The data exclude, at 95% CL, the mass range below 5.3 TeV for the q^* and 7.1 (4.4) TeV for the QBH with six (one) extra dimensions in the Arkani-Hamed–Dimopoulos–Dvali (Randall–Sundrum) model. These limits supersede the previous ATLAS exclusion limits for excited quarks and quantum black holes in the γ + jet final state.

References

[1] U. Baur, I. Hinchliffe, and D. Zeppenfeld. "*Excited Quark Production at Hadron Colliders*". In: *Int. J. Mod. Phys. A* 2 (1987), p. 1285. DOI: 10.1142/S0217751X87000661.

[2] U. Baur, M. Spira, and P. M. Zerwas. "*Excited-quark and -lepton production at hadron colliders*". In: *Phys. Rev. D* 42 (1990), p. 815. DOI: 10.1103/PhysRevD.42.815.

[3] Satyaki Bhattacharya et al. "*Quark excitations through the prism of direct photon plus jet at the LHC*". In: *Phys. Rev. D* 80 (2009), p. 015014. DOI: 10.1103/PhysRevD.80.015014. arXiv: 0901.3927 [hep-ph].

[4] S. Weinberg. "*Gauge Hierarchies*". In: *Phys. Lett. B* 82 (1979), p. 387. DOI: 10.1016/0370-2693(79)90248-X.

[5] M. J. G. Veltman. "*The Infrared - Ultraviolet Connection*". In: *Acta Phys. Polon. B* 12 (1981), p. 437.

[6] C.H. Llewellyn Smith, G. G. Ross. "*The Real Gauge Hierarchy Problem*". In: *Phys. Lett. B* 105 (1981), p. 38. DOI: 10.1016/0370-2693(81)90035-6.

[7] Savas Dimopoulos and Greg L. Landsberg. "*Black holes at the Large Hadron Collider*". In: *Phys. Rev. Lett.* 87 (2001), p. 161602. DOI: 10.1103/PhysRevLett.87.161602. arXiv: hep-ph/0106295.

[8] Steven B. Giddings and Scott D. Thomas. "*High energy colliders as black hole factories: The end of short distance physics*". In: *Phys. Rev. D* 65 (2002), p. 056010. DOI: 10.1103/PhysRevD.65.056010. arXiv: hep-ph/0106219.

[9] Douglas M. Gingrich. "*Quantum black holes with charge, colour, and spin at the LHC*". In: *J. Phys. G* 37 (2010), p. 105008. DOI: 10.1088/0954-3899/37/10/105008. arXiv: 0912.0826 [hep-ph].

[10] Xavier Calmet, Wei Gong, and Stephen D.H. Hsu. "*Colorful quantum black holes at the LHC*". In: *Phys. Lett. B* 668 (2008), p. 20. DOI: 10.1016/j.physletb.2008.08.011. arXiv: 0806.4605 [hep-ph].

[11] Nima Arkani-Hamed, Savas Dimopoulos, and G.R. Dvali. "*The Hierarchy problem and new dimensions at a millimeter*". In: *Phys. Lett. B* 429 (1998), p. 263. DOI: 10.1016/S0370-2693(98)00466-3. arXiv: hep-ph/9803315.

[12] Lisa Randall and Raman Sundrum. "*A Large mass hierarchy from a small extra dimension*". In: *Phys. Rev. Lett.* 83 (1999), p. 3370. DOI: 10.1103/PhysRevLett.83.3370. arXiv: hep-ph/9905221.

[13] Torbjorn Sjöstrand, Stephen Mrenna, and Peter Skands. "*A brief introduction to PYTHIA 8.1*". In: *Comput. Phys. Commun.* 178 (2008), pp. 852–867. DOI: 10.1016/j.cpc.2008.01.036. arXiv: 0710.3820 [hep-ph].

[14] D. M. Gingrich. "*Monte Carlo event generator for black hole production and decay in proton-proton collisions*". In: *Comput. Phys. Commun.* 181 (2010), p. 1917. DOI: 10.1016/j.cpc.2010.07.027. arXiv: 0911.5370 [hep-ph].

[15] ATLAS Collaboration. "*Search for new phenomena with photon+jet events in proton–proton collisions at $\sqrt{s} = 13$ TeV with the ATLAS detector*". In: *JHEP* 03 (2016), p. 041. DOI: 10.1007/JHEP03(2016)041. arXiv: 1512.05910 [hep-ex].

[16] ATLAS Collaboration. "*The ATLAS Experiment at the CERN Large Hadron Collider*". In: *JINST* 3 (2008), S08003. DOI: 10.1088/1748-0221/3/08/S08003.

[17] CMS Collaboration. "*The CMS experiment at the CERN LHC*". In: *JINST* 3 (2008), S08004. DOI: 10.1088/1748-0221/3/08/S08004.

[18] ATLAS Collaboration. "*Search for Production of Resonant States in the Photon-Jet Mass Distribution Using pp Collisions at at $\sqrt{s} = 7$ TeV Collected by the ATLAS Detector*". In: *Phys. Rev. Lett.* 108 (2012), p. 211802. DOI: 10.1103/PhysRevLett.108.211802. arXiv: 1112.3580 [hep-ex].

[19] ATLAS Collaboration. "*Search for new phenomena in photon+jet events collected in proton–proton collisions at $\sqrt{s} = 8$ TeV with the ATLAS detector*". In: *Phys. Lett. B* 728 (2014), p. 562. DOI: 10.1016/j.physletb.2013.12.029. arXiv: 1309.3230 [hep-ex].

[20] CMS Collaboration. "*Search for excited quarks in the γ+jet final state in proton–proton collisions at $\sqrt{s} = 8$ TeV*". In: *Phys. Lett. B* 738 (2014), p. 274. DOI: 10.1016/j.physletb.2014.09.048. arXiv: 1406.5171 [hep-ex].

[21] ATLAS Collaboration. "*Search for New Phenomena in Dijet Mass and Angular Distributions from pp Collisions at $\sqrt{s} = 13$ TeV with the ATLAS Detector*". In: *Phys. Lett. B* 754 (2016), p. 302. DOI: 10.1016/j.physletb.2016.01.032. arXiv: 1512.01530 [hep-ex].

[22] ATLAS Collaboration. "*Search for new phenomena in dijet events using 37 fb^{-1} of pp collision data collected at $\sqrt{s} = 13$ TeV with the ATLAS detector*". In: *Phys. Rev. D* 96 (2017), p. 052004. DOI: 10.1103/PhysRevD.96.052004. arXiv: 1703.09127 [hep-ex].

[23] CMS Collaboration. "*Search for dijet resonances in proton–proton collisions at $\sqrt{s} = 13$ TeV and constraints on dark matter and other models*". In: *Phys. Lett. B* 769 (2017), p. 520. DOI: 10.1016/j.physletb.2017.02.012. arXiv: 1611.03568 [hep-ex].

[24] ATLAS Collaboration. "*Search for new phenomena in high-mass final states with a photon and a jet from pp collisions at $\sqrt{s} = 13$ TeV with the ATLAS detector*". In: *Eur. Phys. J. C* 78 (2018), p. 102. DOI: 10.1140/epjc/s10052-018-5553-2. arXiv: 1709.10440 [hep-ex].

[25] ATLAS Collaboration. "*Performance of the ATLAS trigger system in 2015*". In: *Eur. Phys. J. C* 77 (2017), p. 317. DOI: 10.1140/epjc/s10052-017-4852-3. arXiv: 1611.09661 [hep-ex].

[26] ATLAS Collaboration. "*Measurement of the photon identification efficiencies with the ATLAS detector using LHC Run-1 data*". In: *Eur. Phys. J. C* 76 (2016), p. 666. DOI: 10.1140/epjc/s10052-016-4507-9. arXiv: 1606.01813 [hep-ex].

[27] ATLAS Collaboration. "*Measurement of the inclusive isolated prompt photon cross section in pp collisions at $\sqrt{s} = 7$ TeV with the ATLAS detector*". In: *Phys. Rev. D* 83 (2011), p. 052005. DOI: 10.1103/PhysRevD.83.052005. arXiv: 1012.4389 [hep-ex].

[28] ATLAS Collaboration. "*Jet energy scale measurements and their systematic uncertainties in proton–proton collisions at* $\sqrt{s} = 13$ *TeV with the ATLAS detector*". In: *Phys. Rev. D* 96 (2017), p. 072002. DOI: 10.1103/PhysRevD.96.072002. arXiv: 1703.09665 [hep-ex].

[29] ATLAS Collaboration. "*Tagging and suppression of pileup jets with the ATLAS detector*". In: (2014). ATLAS-CONF-2014-018. URL: https://cds.cern.ch/record/1700870.

[30] ATLAS Collaboration. "*Selection of jets produced in* 13 *TeV proton–proton collisions with the ATLAS detector*". In: (2015). ATLAS-CONF-2015-029. URL: https://cds.cern.ch/record/2037702.

[31] Kyle S. Cranmer. "*Kernel estimation in high-energy physics*". In: *Comput. Phys. Commun.* 136 (2001), pp. 198–207. DOI: 10.1016/S0010-4655(00)00243-5. arXiv: hep-ex/0011057.

[32] Max Baak et al. "*Interpolation between multi-dimensional histograms using a new non-linear moment morphing method*". In: *Nucl. Instrum. Meth. A* 771 (2015), pp. 39–48. DOI: 10.1016/j.nima.2014.10.033. arXiv: 1410.7388 [physics.data-an].

[33] ATLAS Collaboration. "*Search for dark matter at* $\sqrt{s} = 13$ *TeV in final states containing an energetic photon and large missing transverse momentum with the ATLAS detector*". In: *Eur. Phys. J. C* 77 (2017), p. 393. DOI: 10.1140/epjc/s10052-017-4965-8. arXiv: 1704.03848 [hep-ex].

[34] ATLAS Collaboration. *ATLAS Public Web*. URL: https://atlas.web.cern.ch/Atlas/GROUPS/PHYSICS/PAPERS/EXOT-2016-26/.

[35] S. Catani et al. "*Cross-section of isolated prompt photons in hadron hadron collisions*". In: *JHEP* 05 (2002), p. 028. DOI: 10.1088/1126-6708/2002/05/028. arXiv: hep-ph/0204023.

[36] T. Gleisberg et al. "*Event generation with SHERPA 1.1*". In: *JHEP* 02 (2009), p. 007. DOI: 10.1088/1126-6708/2009/02/007. arXiv: 0811.4622 [hep-ph].

[37] R. A. Fisher. "*On the Interpretation of* χ^2 *from Contingency Tables, and the Calculation of P*". In: *J. Royal Statistical Society* 85 (1922), p. 87. DOI: 10.2307/2340521.